High-resolution structures of the Landers fault zone inferred from aftershock waveform data

Hongyi Li,* Lupei Zhu and Hongfeng Yang

Department of Earth and Atmospheric Sciences, Saint Louis University, St Louis, MO 63108, USA. E-mail: lupei@eas.slu.edu

SUMMARY

High-frequency body waves recorded by a temporary seismic array across the surface rupture trace of the 1992 Landers, California, earthquake were used to determine fault-zone structures down to the seismogenic depth. We first developed a technique to use generalized ray theory to compute synthetic seismograms for arbitrarily oriented tabular low-velocity fault-zone models. We then generated synthetic waveform record sections of a linear array across a vertical fault zone. They show that both arrival times and waveforms of *P* and *S* waves vary systematically across the fault due to transmissions and reflections from boundaries of the low-velocity fault zone. The waveform characteristics and arrival-time patterns in the record sections allow us to locate the boundaries of the fault zone and to determine its *P*- and *S*-wave velocities independently as well as its depth extent. Therefore, the trade-off between the fault-zone width and velocities can be avoided. Applying the method to the Landers waveform data reveals a low-velocity zone with a width of 270–360 m and a 35–60 per cent reduction in *P* and *S* velocities relative to the host rock. The analysis suggests that the low-velocity zone extends to a depth of ∼7 km. The western boundary of the low-velocity zone coincides with the observed main surface rupture trace.

Key words: fault model, fracture zone, ray theory, reflection seismology, seismic modelling, seismic-wave propagation.

GJI Seismology

1 INTRODUCTION

Earthquakes are the result of rapid movement of crustal blocks on faults. Studies of faults exposed on the surface indicate that a fault is not a simple plane embedded in the crust but is marked by a narrow zone called a *fault zone* (FZ) with a finite width. The primary components of a FZ are a fault core in the centre and a damage zone which bounds the fault core (e.g. Ben-Zion & Sammis 2003). Often the fault core consists of a narrow layer (tens of centimetres to several meters) of cataclasite and ultracataclasite that accommodates most of the slip. The damage zone is characterized by localized zones of fractures and subsidiary faults that are several 100 m in thickness (e.g. Chester *et al.* 1993; Evans & Chester 1995; Chester & Chester 1998). Most earthquake rupture models, including the asperity, barrier and stick-slip paradigms, suggest that FZ structure (geometrical and material properties) controls the earthquake rupture process and may hold the key to understanding the earthquake physics (Aki 1979; Scholz 1990; Kanamori 1994; Kanamori & Brodsky 2004). Unfortunately, to determine those properties of the FZ at seismogenic depths where earthquakes nucleate and the

majority of slip occurs has been shown to be extremely difficult (McGuire & Ben-Zion 2005).

Geological studies of exhumed faults provide detailed information on inactive FZs that were, at one time, at various depths. Drilling in an active FZ, such as the SAFOD project, allows direct samplings of the FZ but the coverage is limited both vertically (a few kilometres) and laterally (one point measurement). The seismic reflection technique is not particularly effective in imaging steep faults and so far only a few successful cases of illuminating the shallow part (<4 km) of a FZ have been reported (e.g. Louie *et al.* 1988; Korneev *et al.* 2000; Hole *et al.* 2001; Chavarria *et al.* 2003; Maercklin *et al.* 2004). To study FZs to the base of the seismogenic layer, various geophysical methods such as gravity, electromagnetic and seismic methods have been applied. Among those, modelling seismic waveforms recorded by stations near FZs provides the highest resolution. So far, most efforts have been focused on modelling the so-called FZ trapped waves, which are large-amplitude and low-frequency (2–5 Hz) wave trains that follow the *S* wave (e.g. Ben-Zion & Aki 1990; Li & Leary 1990; Li *et al.* 1994; Ben-Zion *et al.* 2003). In several cases, a low-velocity zone of ∼100 m wide down to seismogenic depths (10–18 km) is reported based on forward modelling of these long-period waves (e.g Li *et al.* 1994; Li & Vernon 2001; Li *et al.* 2004). However, it is still debated whether these wave trains are generated in a layer that extends to the bottom of the seismogenic zone, or in a 3–4-km-deep damage structure that is largely above the

*Now at: School of Geophysics and Geoinformation Systems, China University of Geosciences, Beijing, China.

1

seismicity (Ben-Zion *et al.* 2003). Numerical simulations showed that shallow FZ layers can produce ample trapped wave energy by earthquakes well outside and below the FZ (Jahnke *et al.* 2002; Fohrmann *et al.* 2004). This has put questions on the effectiveness of the technique for characterization the FZ at depth. In addition, there are considerable uncertainties with trapped-wave modelling results due to non-uniqueness and trade-offs among different FZ parameters (Ben-Zion 1998; Peng *et al.* 2003; Lewis *et al.* 2005). In order to resolve these important issues and be able to move forward, we have to explore other features in seismic waveforms and develop new techniques to improve resolution and reduce non-uniqueness.

A very valuable, but so far relatively underutilized seismic data set in FZ structure modelling is the *P* and *S* body waves generated by aftershocks in and near the FZ. Body waves have higher frequency content and the ability to sample greater depths than are the long-period trapped waves. There have been a few studies of using FZ generated head waves to determine velocity contrasts of FZ and lateral variations (Ben-Zion 1989; Ben-Zion & Aki 1990; Ben-Zion & Malin 1991; Hough *et al.* 1994; McGuire & Ben-Zion 2005). In this study, we will use *P* and *S* body-wave waveforms from aftershocks recorded by a temporary seismic array following the 1992 Landers, California, earthquake to determine the Landers FZ structure. We will first describe an efficient method to compute synthetic seismograms of an arbitrarily oriented FZ model based on generalized ray theory. Waveform characteristics from a simple FZ model will be analysed. We then use the method to determine FZ parameters (strike, width, velocities and depth extent) of the Landers FZ.

2 METHOD

2.1 Computing synthetic seismograms of FZ models using generalized ray theory

For computing synthetic seismograms in different FZ models, the finite-difference (FD) technique is often used. That method is, however, computationally intensive and requires long computer CPU time and large memory storage, especially when using high-frequency signals. In contrast, generalized ray theory (GRT) computes seismograms in the time-domain semi-analytically (Helmberger 1983), and is, therefore, very fast. The highest frequency of GRT seismograms is only limited by the time sampling rate and can easily go above 10 Hz without demanding large memory storage. More importantly, GRT decomposes a seismogram into responses of many individual generalized rays, allowing kinematic and dynamic properties of different seismic phases in the seismogram to be isolated and analysed.

Application of GRT has usually been limited to horizontally layered velocity models. Ben-Zion (1989, 1990) and Ben-Zion & Aki (1990) have developed algorithms utilizing GRT to study FZ structure. Their methods, however, are either only applicable to the fault-parallel component of seismograms for a vertical FZ or limited to a structure of two different half spaces. In this study, we have developed a method that rotates a FZ model to a horizontal layered model and then uses GRT to compute synthetic seismograms.

In a tabular FZ model, a low-velocity layer is embedded in a uniform half-space (Fig. 1). Using the fault normal vector $\hat{N}$ and the vector $\vec{r}$ pointing from the source to the station, we can derive two mutually perpendicular unit vectors:

$$\hat{T} = \frac{\hat{N} \times \vec{r}}{|\hat{N} \times \vec{r}|}, \tag{1}$$
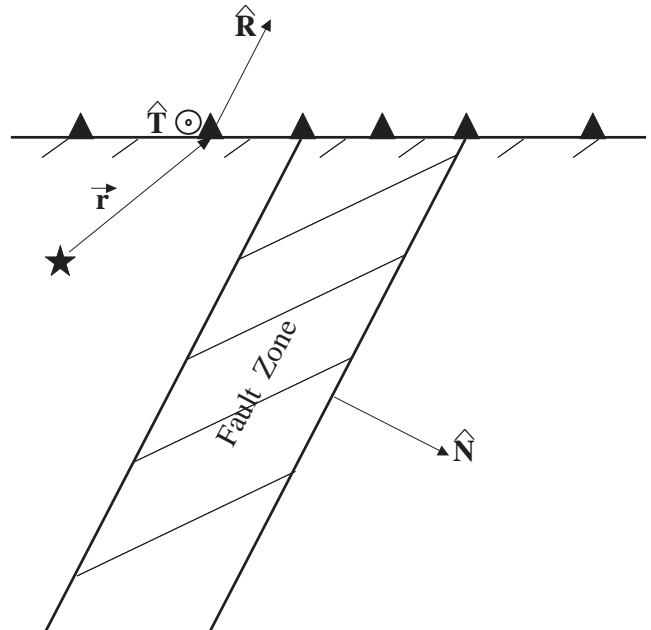
Figure 1. An arbitrarily oriented tabular FZ model. The star denotes an earthquake and triangles represent stations.

$$\hat{R} = \hat{T} \times \hat{N}. \tag{2}$$

The three vectors, $\hat{R}$, $\hat{T}$ and $\hat{N}$, form a right-hand orthogonal vector base. In this coordinate system, the FZ lies horizontally with $\hat{N}$ pointing downward. $\hat{R}$ is the radial direction at the station and $\hat{T}$ is the transverse direction. In the case of a vertical FZ, $\hat{T}$ is often referred as the fault-parallel direction and $\hat{N}$ as the fault-normal direction.

In order to use GRT, we must ignore the free surface. Synthetic seismograms are computed using the whole-space receiver functions at the location of the station. We correct seismograms for the free-surface effect by multiplying them by the ratios of half-space receiver functions and whole-space receiver functions. For the *SH*-component, the ratio is 2. For the *P–SV* waves, the ratios vary with the ray parameter, but are close to 2 when the incident angle is small (Helmberger 1983). For most FZ studies using aftershocks, the events used are usually very close to seismic stations and the seismic rays have steep incident angles. So the approximation is reasonably justified.

We compared GRT seismograms for a simple FZ model with those obtained using the FD technique (Fig. 2). It is seen that the agreement between the two sets of synthetics is reasonably good, particularly for the body waves, in terms of both amplitude and waveform shape. For the FD method, we used a time step of 0.002 s and a grid spacing of 30 m, which gives a maximum frequency of 15 Hz. It took about 3 hr to compute on a 16-node Linux cluster with dual AMD 2.8 MHz CPUs at each node. The GRT algorithm only took a few seconds using a single node.

2.2 Waveform characteristics of a simple FZ model

With the aid of the GRT and FD methods, waveform characteristics of different FZ models can be investigated. We set up a simplified FZ model that consists of a 300-m-wide vertical low-velocity zone embedded in a half-space. The *P*- and *S*-wave velocities of the half-space are 6.3 and 3.6 km s^{-1}, respectively. The FZ has a velocity

Inside

N

T

S

R

P

Outside

N

T

S

R

P

0   1   2

t (s)
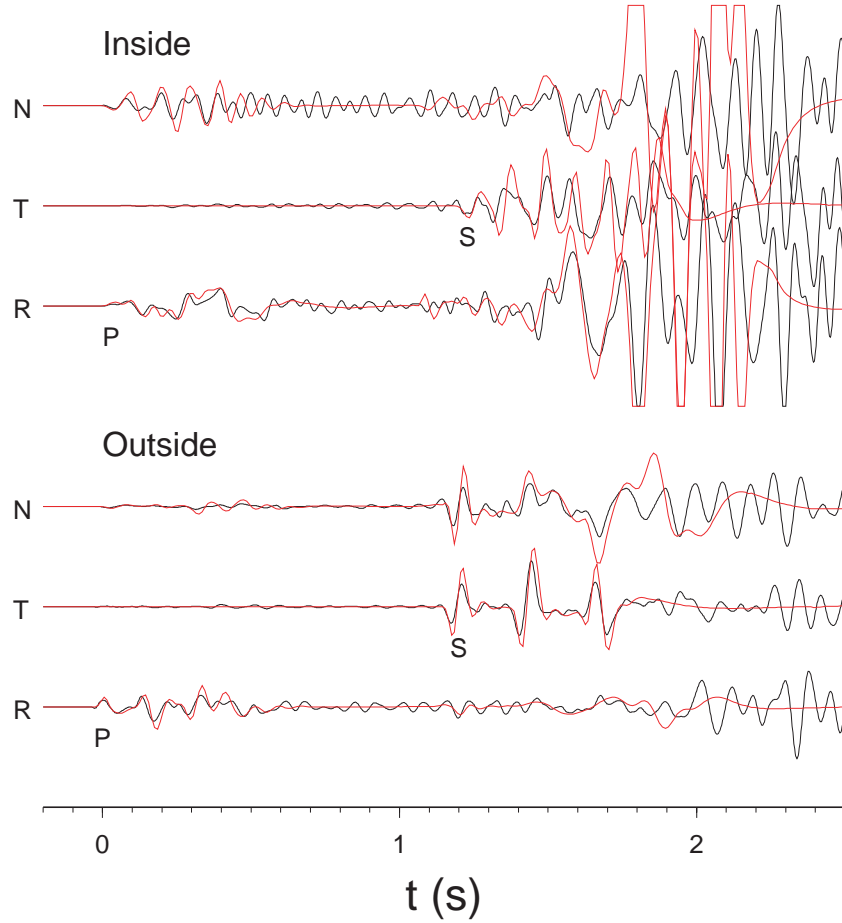
Figure 2. Comparisons of synthetic seismograms obtained by the FD (black line) and the GRT (red line) methods for stations outside and inside a 300-m-wide FZ with a 40 per cent drop in both P and S velocities. The earthquake is 4 km away from the stations and 9 km deep.

drop of 40 per cent in both P and S-wave velocities and a 30 per cent decrease in density with respect to the host rock. Its Q values are 120 (Q_p) and 60 (Q_s), while the Q values are 300 and 150 in the host rock. The orientation of the FZ is N–S and a linear seismic array of 1.5 km long is deployed across the FZ (see Fig. 3).

Fig. 3 shows GRT synthetic seismograms from an earthquake located outside the FZ (1 km to the western boundary). The event is 9 km deep and 4.0 km in epicentral distance to the centre station of the array. Because of the low-velocity FZ, the first P and S arrivals at the eastern stations are delayed. Also plotted are arrival times of major body-wave phases calculated by GRT. Their corresponding ray paths are shown on the left-hand side. It shows that those coherent phases following the direct P and S waves are multiple internal reflections from boundaries of the FZ. Here we label them as P^2, S^2, P^4, S^4 and so on, where the superscript indicates the number of additional ray path legs in the FZ. For stations located outside the FZ, the multiple reflections are nearly evenly spaced and show little moveout with respect to the direct arrivals. For stations located within the FZ, the forward and backward reflections at the western and eastern boundaries of the FZ have the opposite traveltime moveouts, forming a characteristic 'V'-shaped pattern (Fig. 3).

Waveform characteristics from events inside the FZ are drastically different. Fig. 4 shows a record section for an event located in the middle of the 300-m-wide FZ. The multiple internal reflections are more closely spaced. For stations located within the FZ, the arrival-time curves of the multiple internal reflections crisscross to form a

distinctive 'X'-shaped pattern. Compared to the previous case of an outside event, the number of reflection phases is doubled. This is because that in addition to travelling to a station directly (as P and S) and by FZ internal reflections (as P^2, P^4, S^2, S^4, etc.), seismic rays can also leave the source in the opposite direction and be reflected from the FZ boundary. This additional group of phases is similar to the depth phase produced by reflection at the Earth's surface above teleseismic earthquakes, except that the 'depth' in our case is the distance of the source to the FZ boundary. Accordingly, we label these additional phases pP, sS, pP^2, sS^2, pP^4, sS^4 and so on.

The above observations allow us to design a strategy to determine the FZ width and velocities separately. The locations of the FZ boundaries are found by identifying places in the waveform record section where there is an abrupt change in the slope of the direct arrival times and a bifurcation of a reflection branch from stations outside the FZ to stations inside (Fig. 3). The FZ velocities, V_p and V_s, can be determined by the slope of the direct arrival times at stations located inside the FZ. In addition, the width w and velocities can be further constrained by the time separations between a multiple reflection and the direct arrival. When the event is close to the FZ, the time separation can be expressed as:

$$P^n - P = nw\sqrt{V_p^{-2} - p^2}, \qquad (3)$$

$$S^n - S = nw\sqrt{V_s^{-2} - p^2}, \qquad (4)$$
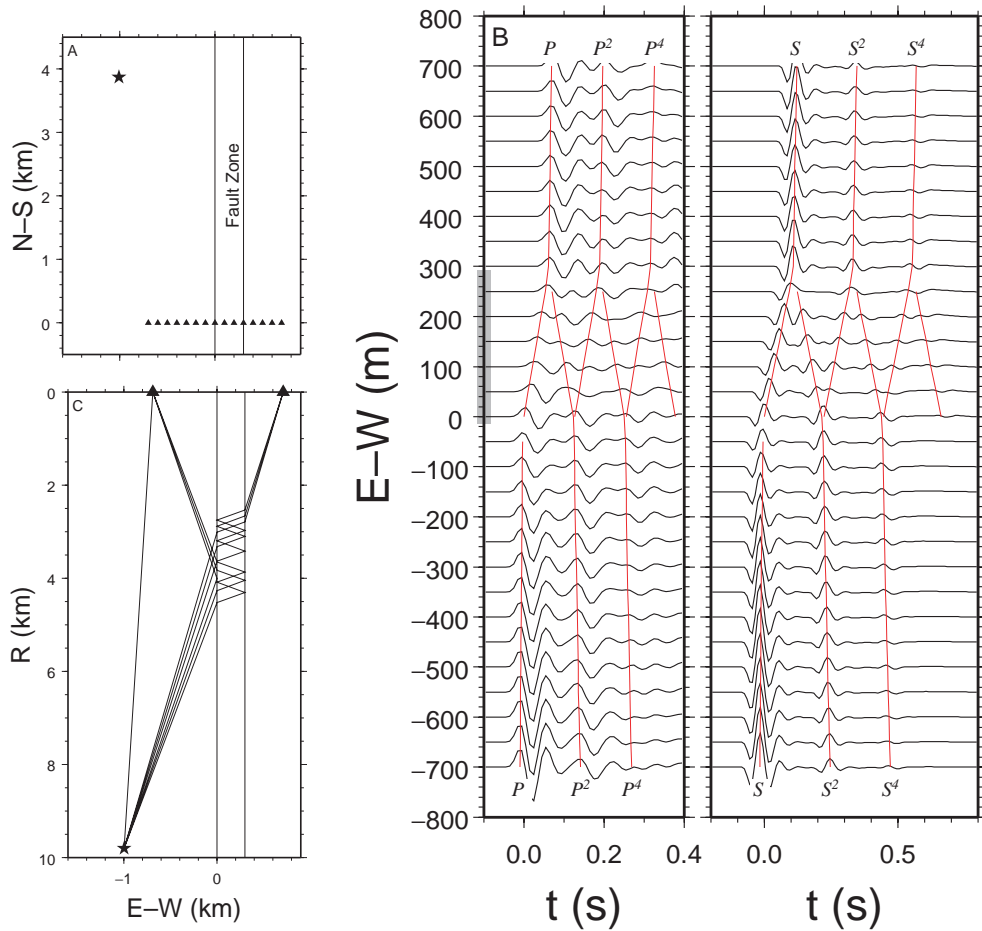
Figure 3. (a) Location of a linear seismic array (triangles) across a 300-m-wide FZ. The earthquake (star) is located 1 km outside to the western boundary of the FZ. (b) The vertical (left-hand panel) and fault-parallel (right-hand panel) components of seismograms of the linear array. The location of the FZ on the profile is indicated by the grey-coloured bar. Arrival times of major body-wave phases are shown in red-coloured lines. Their ray paths to two stations are shown in (c).

where p is the ray parameter and n is the number of ray legs of the multiple reflection in the FZ. A big advantage of this method over other techniques such as the trapped-wave modelling is that it eliminates the trade-off between the FZ width and velocities because the width is determined independent of the FZ velocities. Furthermore, it is feasible to estimate the density contrast at the FZ boundaries by using the amplitudes of FZ reflections.

Using differential arrival times between the direct arrival and the multiple reflections to determine the FZ velocities also greatly reduces the influence of event location uncertainty. When the event is near (inside or outside) the FZ, the ray parameter p and, therefore, the time separations between the direct and the reflected phases change negligibly by event location perturbation. This is demonstrated by nearly the same separation between those phases in Figs 3 and 4. On the other hand, for the inside events, the separation between P and the 'depth' phase pP (similarly $sS - S$) is very sensitive to the relative distance of the event to the FZ boundaries. This gives us a powerful tool to locate the event relative to the FZ boundaries with great accuracy and confidence.

Determining FZ width and velocities by modelling FZ reflected waves also provides much better depth resolution of FZ structure. The parameters obtained by using P^2 and S^2 should represent FZ structure around the reflection points. For the inside earthquakes, the reflection points are right above the hypocenter (Fig. 4). For

the outside earthquakes, the depth range of the FZ sampled by the reflections depends on the depth of the earthquake and the relative distances of the event and station to the FZ. For a 1.5-km-long linear array across a FZ, reflection points from an event 9 km deep and 1 km away from the FZ can be as deep as 5 km (Fig. 3). As the source moves closer to the FZ, the sampled depth range becomes deeper.

To test whether the above approach can differentiate a shallow low-velocity FZ model from a one that extends to the base of the seismogenic zone, we computed synthetics for FZ model terminated at different depths using the FD method. The width, velocity drops and Q values of the FZ have been kept the same. Fig. 5(a) shows a waveform record section for a FZ extending to a depth of 7 km from the outside event. The waveforms are almost identical to those of the deep FZ model in Fig. 3. This is expected because, as we have pointed out above, the depth range of the FZ sampled by the seismic rays from the event is above the 7-km termination depth (Fig. 3c). When the FZ is terminated at a depth of 5 km, noticeable differences can be observed in the record section (Fig. 5b). The amplitudes of FZ reflections recorded by stations away from the FZ are smaller. More importantly, we see a weak diffracted arrival before the predicted P arrival at eastern stations (indicated by the arrow in Fig. 5b). If the low-velocity FZ extends only to a depth of 3 km, the corresponding waveform record section is clearly different from those of deeper FZ models (Fig. 5c). Only stations located inside the FZ show clear
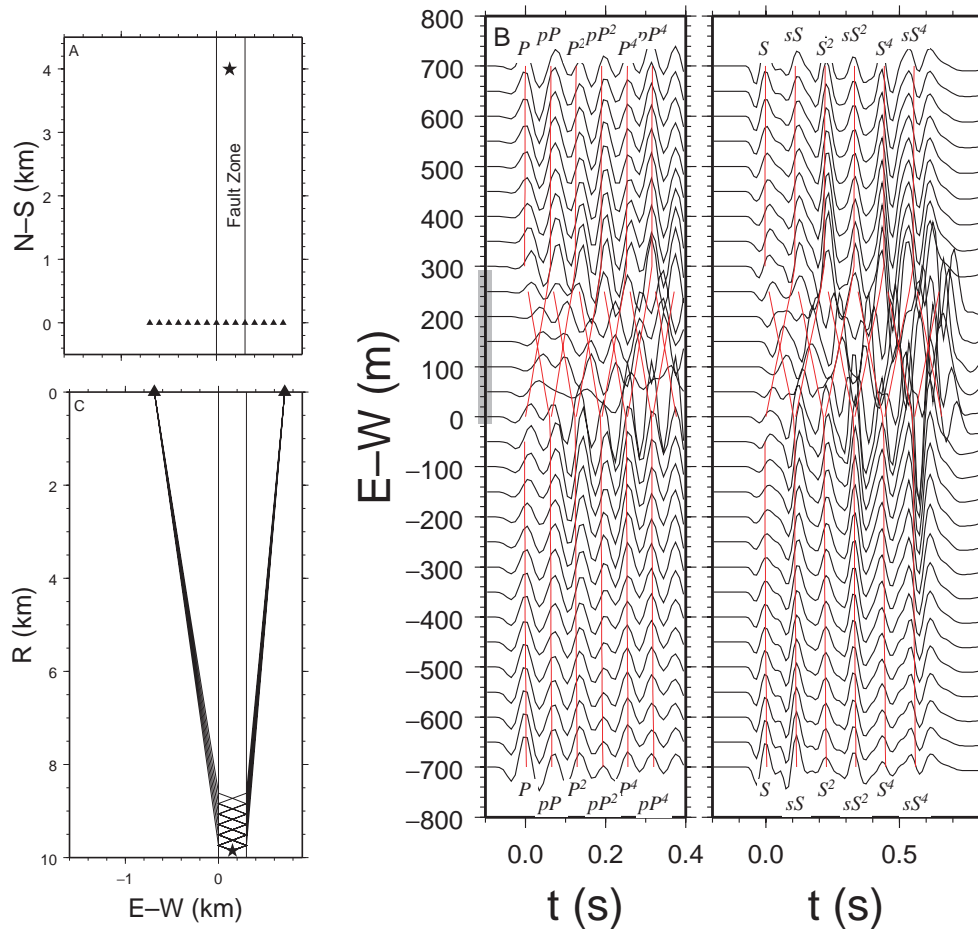
Figure 4. Same as in Fig. 3 for an earthquake located in the middle of the FZ.

delays in direct arrival times. This makes the record section look like the one in Fig. 4 from an event inside a deep FZ. Indeed, the secondary arrivals at the eastern stations in Fig. 5(c) can be easily misinterpreted as the 'depth' phase pP and be erroneously used to locate the event inside the FZ.

We therefore, conclude that shallow aftershocks or events far away from the FZ provide little information about the depth extent of the FZ. The best evidence for a deep low-velocity FZ are asymmetric waveform record sections like the one in Fig. 3 from deep events close to the FZ. Waveform record sections with symmetric arrival times across the fault trace, such as the one in Fig. 4, do not necessarily indicate a deep FZ even if the events are deep because they may be produced, as shown here and in Fohrmann *et al.* (2004), by aftershocks beneath a shallow low-velocity FZ.

3 DATA AND RESULTS

The 1992 June 28, Landers, California, earthquake was the largest (M_w 7.3) earthquake in southern California since the 1952 M_w 7.7 Kern County event. The epicentre is 8 km south-southwest of the town of Landers (Fig. 6). It ruptured five previously recognized major faults with a total length of about 85 km. The horizontal offset along the fault trace was typically 2–3 m, with the maximum offset around 6 m (Sieh *et al.* 1993).

After the earthquake, several dense temporary seismic arrays were deployed along the main shock surface rupture. In October 1992,

six portable stations were deployed at a site 9 km north of the main shock epicentre (Li *et al.* 1994) (Fig. 6). During the same time period, a PC-based portable seismic array was also deployed (Lee 1999). It consisted of 31 three-component, short-period seismometers. 22 stations formed a 1-km-long east–west line along the Encantada Road. The line was centred at the surface rupture trace and the station spacing varies from 25 m within 200 m of the surface breakage to 50–100 m outside. In this study, we combined the data from the two arrays for analysis.

The PC-based array was in operation for 7 d and recorded a total of 238 aftershocks. 93 of those aftershocks were also recorded by the Southern California Seismic Network (SCSN) and have been located by Shearer *et al.* (2005). Fig. 7 shows locations of aftershocks that are within ∼5 km in epicentral distance to the array. We examined their waveform record sections along the E–W line across the fault trace. We first removed instrument responses from the records and bandpass filtered them between 1 and 15 Hz. We then rotated the three components of the records to the *R*, *T* and *N* directions by assuming that the fault zone is vertical and strikes N5°W, which follows the trend of the surface rupture traces in our study area (Fig. 7). Figs 8–11 show record sections of four events. Event 50829 is located SW of the array at a depth of 3.8 km. A notable feature of the record section is that *P* arrival times at the eastern stations are delayed by ∼0.1 s (Fig. 8). The delays occur over a distance of ∼300 m along the profile, starting near station C00 and ending near station E07. Similar delay pattern can be observed for a deeper (11.3 km) event 40228 from the same direction
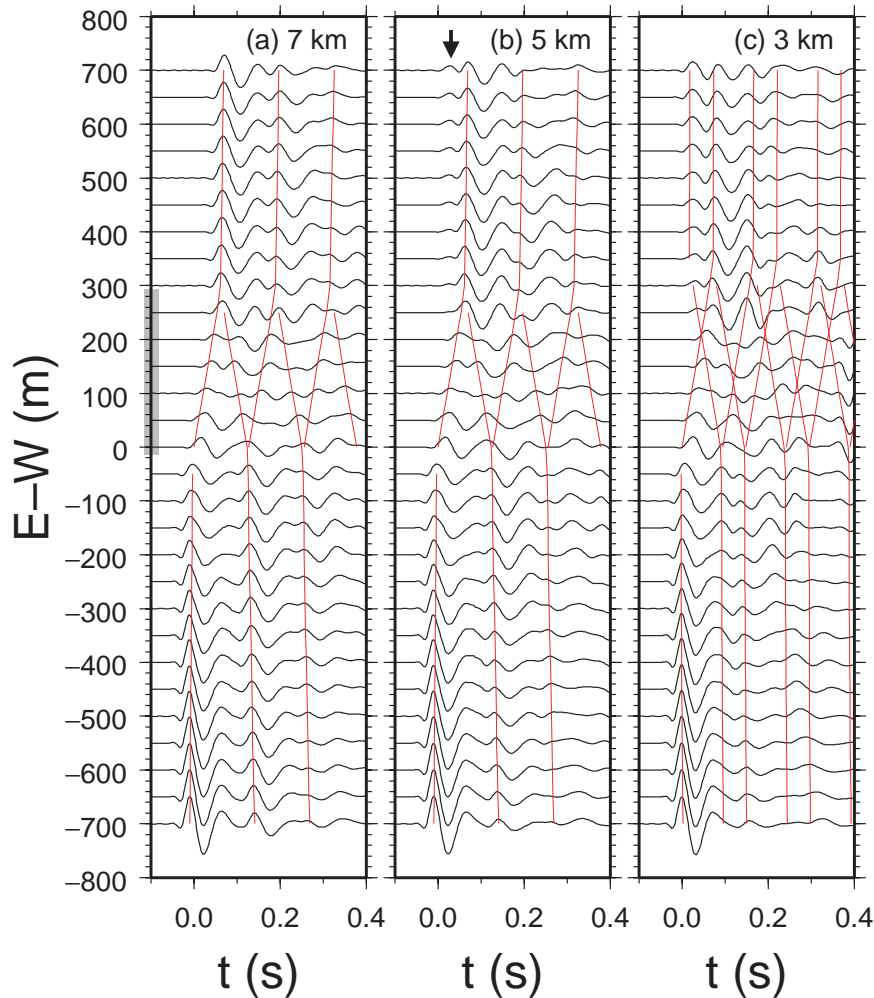
Figure 5. Same as in Fig. 3 except that the FZ is terminated at a depth of (a) 7 km, (b) 5 km and (c) 3 km. Only the *P* wave (the vertical component) record sections are shown here. The predicted arrival times (red lines) are calculated using the deep FZ model with the same event location (in a and b) and with the event in the FZ (in c).

(Fig. 9). For event 40553 from the east side of the fault trace, the western stations are relatively delayed (Fig. 10). Event 40028 is located south of the array (Fig. 7). *P* and *S* arrival times at the western and eastern stations are similar, but they are delayed in the central portion of the profile (Fig. 11). These observations indicate that the fault zone in our study area is associated with a low-velocity zone of ∼300 m in width. Interestingly, the low-velocity zone is not centred at the surface rupture trace but is shifted to the east, which was also found in the trapped wave inversion of Peng *et al.* (2003).

We hand-picked *P* arrival times at each station for all located aftershocks and calculated their traveltime residuals using a 1-D crustal velocity model. We then calculated station delays by averaging all traveltime residuals. Their distribution also suggests a low-velocity zone of ∼300 m in width following the surface rupture traces (Fig. 7).

We used GRT to model waveform record sections of 10 aftershocks that are within 5 km in epicentral distance to the array. Their initial epicentral locations were taken from the results of Shearer *et al.* (2005) while their depths were recalculated from the measured *S–P* times at the array. The FZ model consists of a low-velocity zone in a host rock of 6.3 km s^{-1} in V_p and 3.6 km s^{-1} in V_s. The FZ *P* and *S* velocities and the width were determined by a least-squares

inversion of the observed *P* and *S* arrival times. When FZ reflected phases could be identified in the record sections, which was the case for most events, we included the time separations between the direct and the reflected arrivals in the inversion. The locations of the FZ's western and eastern boundaries were constrained by identifying places in the waveform record section where there is an abrupt change in the slope of the direct arrival times. To take into consideration the uncertainties in event location and FZ orientation, we repeated the inversion 500 times while randomly perturbing the event location within 2 km from its catalogue location, the FZ strike within 15° from N5°W, and the FZ dip within 5° from the vertical. The final 'optimal' parameters were obtained by the average of all acceptable solutions, weighted using the rms of traveltime residuals. An example is presented in Fig. 12 using event 40228. It shows that the FZ velocities and width can be constrained tightly using arrival times of the direct and FZ reflected phases, even though the event location and FZ orientation are not well constrained and have large uncertainties. The inversion results for all 10 events are listed in Table 1. The obtained FZ velocity-drops with respect to the host rock range from 34 to 53 per cent in *P* velocity and from 40 to 59 per cent in *S* velocity. The width of the fault zone varies from 275 to 365 m. Samples of arrival time fits produced by the obtained FZ
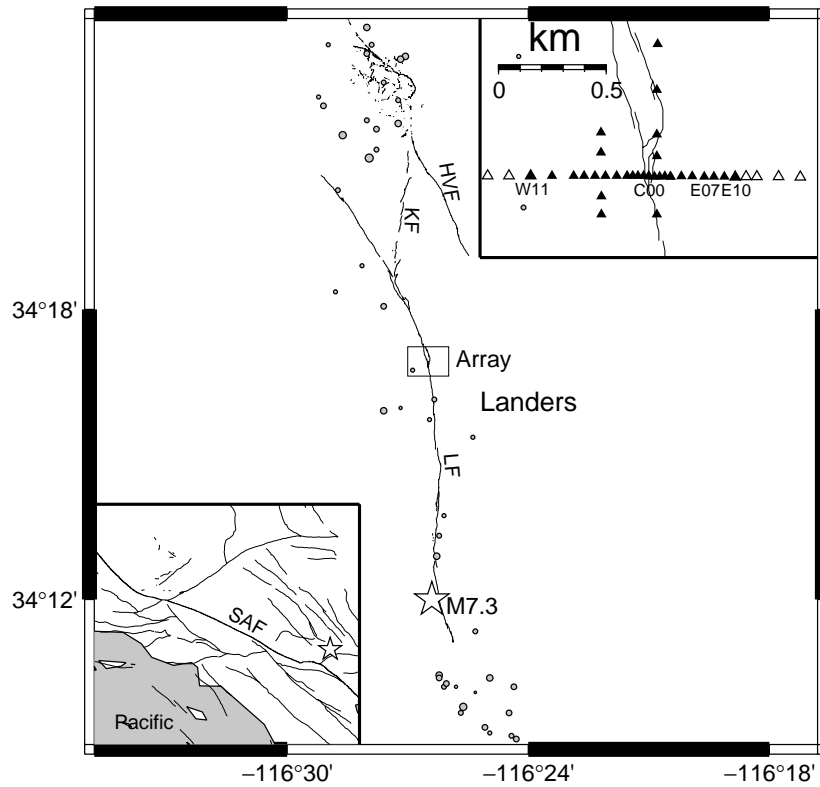
Figure 6. Surface ruptures produced by the Landers earthquakes, LF: the Landers fault; KF: the Kickapoo fault; HVF: the Homestead Valley fault. The inserted map on the top-right shows locations of temporary seismic stations of Lee (1999) (darkened triangles) and Li *et al.* (1994) (open triangles).
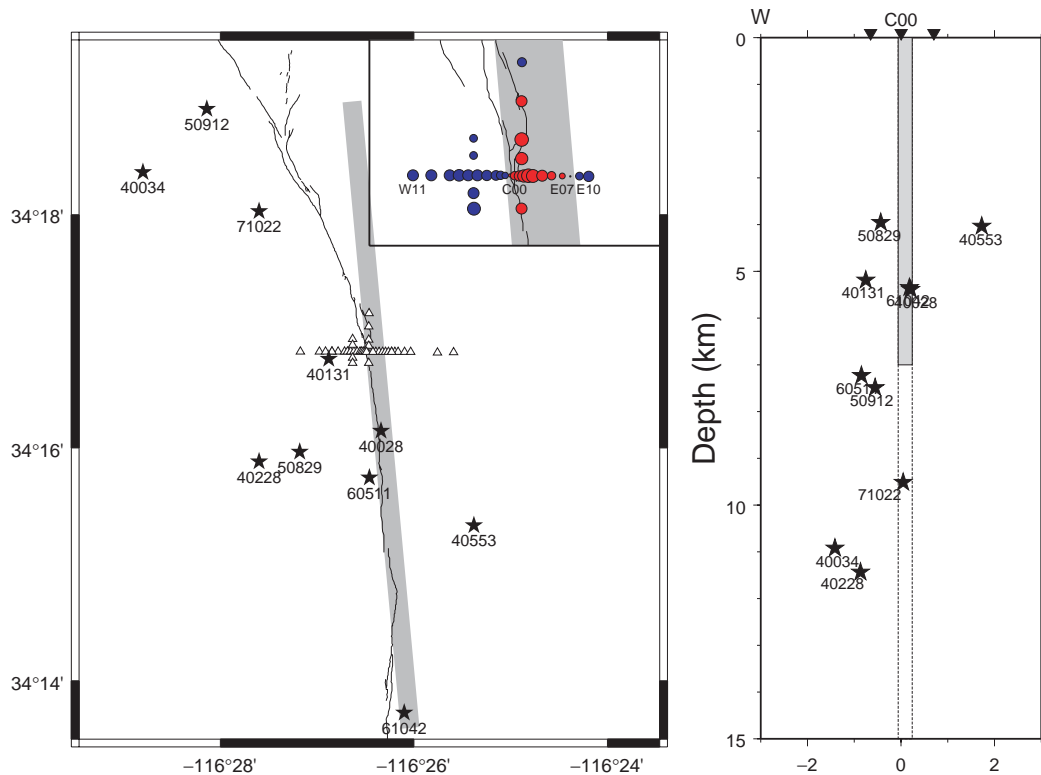
Figure 7. The left-hand panel shows aftershock locations (stars) recorded by the array (triangles). The thickened grey-coloured line represents a straight idealized FZ striking N5°W following the trend of surface rupture traces and seismicity near the array. The inset map shows station delays by averaging *P*-wave traveltime residuals with respect to a 1-D velocity model from all located events. Red represents positive delays and blue negative delays. Their sizes are proportional to the size of the delay. The right-hand panel shows projections of the relocated events and the FZ on to a vertical cross-section perpendicular to the strike of the FZ.

50829 3.8 km
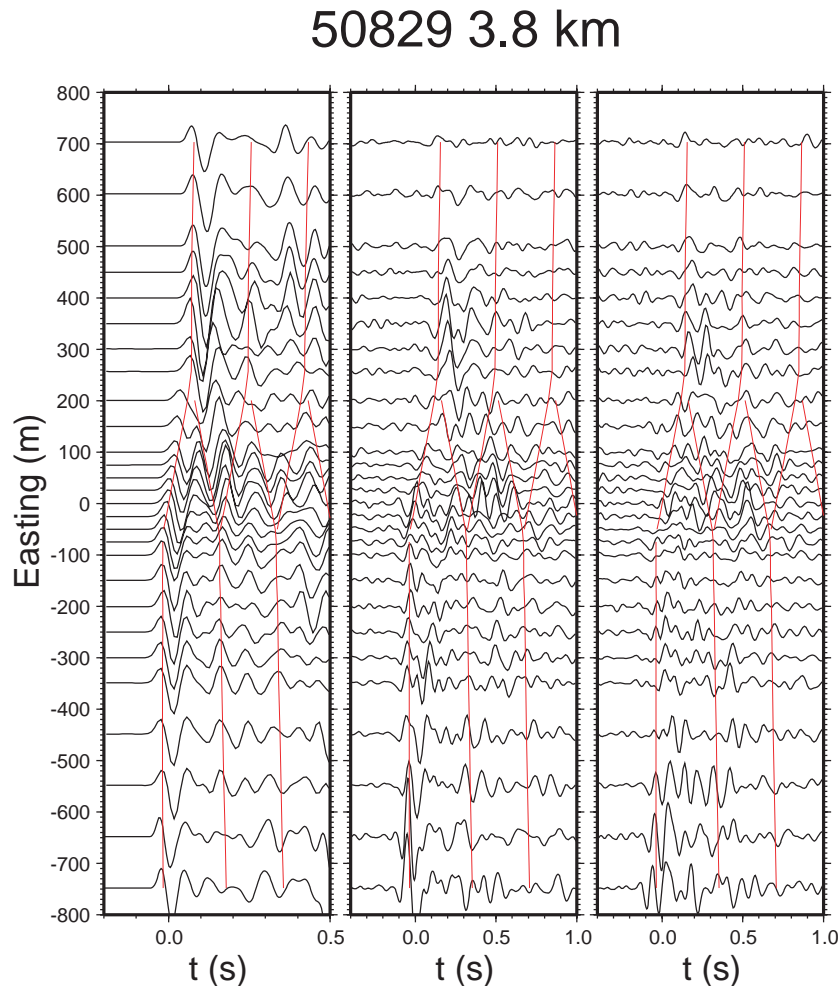
Figure 8. Waveform record sections of, from the left- to right-hand side, radial, fault-normal, and fault-parallel components for event 50829. The event depth is displayed on the top. The horizontal axes show time after the *P* arrival at station C00 for the radial component and after the *S* for the fault-normal and fault-parallel components. The red-colour lines represent predicted arrival times of *P* or *S* and its multiple FZ reflection phases using the FZ parameters obtained in this study.

models are shown in Figs 8–11. It can be seen that we have achieved good agreements between the observed and predicted arrival times of the direct as well as the FZ reflected phases. For some events we were able to fit arrival times of the FZ reflected phases to the second order (P^4 and S^4), see Figs 8 and 9, for examples. As pointed out in the Method section, the arrival time separations between the direct and the FZ reflected phases are more reliable for constraining the FZ width and velocities because they are insensitive to events' mislocations and host rock velocities.

In addition to fitting arrival times of the direct and reflected phases, we also used synthetic seismograms to verify the obtained FZ models. The attenuation factors in the FZ are 60 and 30 for Q_p and Q_s, respectively, and 100 (Q_p) and 50 (Q_s) outside the FZ. We determined the moment tensor of each event using the Cut-and-Paste (CAP) method of Zhu & Helmberger (1996). The moment magnitudes (M_w) we obtained for the events are listed in Table 1. Fig. 13 shows an example of waveform fits for event 40034. Good waveform matches have been achieved between the observations and GRT synthetics for the direct *P* and *S* waves and the FZ reflected waves P^2 and S^2. The fits deteriorate for the late part of the waveforms, most likely due to vertical and lateral variation of

FZ structure. We also found that lower FZ Q_p of 40 would knock down the amplitudes of FZ reflected waves too much when compared to the observation. This implies that either the actual Q values are higher or the propagation distance involving the fault zone is shorter. Resolution of the most likely Q values and associated constrains on the depth extent of the damage zone is left for a future work.

Among the 10 aftershocks we modelled, seven are located outside the FZ. Their distances to the western boundary of the FZ range from 20 m to 1 km (Fig. 7) and FZ reflections from these events recorded by the array sample the FZ at different locations down to a depth of ~6 km (Table 1 and Fig. 14). The inversion results suggest that the FZ structure varies laterally and with depth. Fig. 14 shows that in general both the FZ width and velocities decrease with depth. To determine how deep the low-velocity FZ extends, we terminated it at different depths and computed synthetic waveform record sections of the events using the FD method. We found that if the termination depth is shallower than 7 km, a diffracted precursor appears before the direct arrival at stations across the FZ from those deep outside events (40034, 40228 and 50912), as demonstrated previously in Fig. 5(b). Only the record section from the deepest event

40228 11.3 km
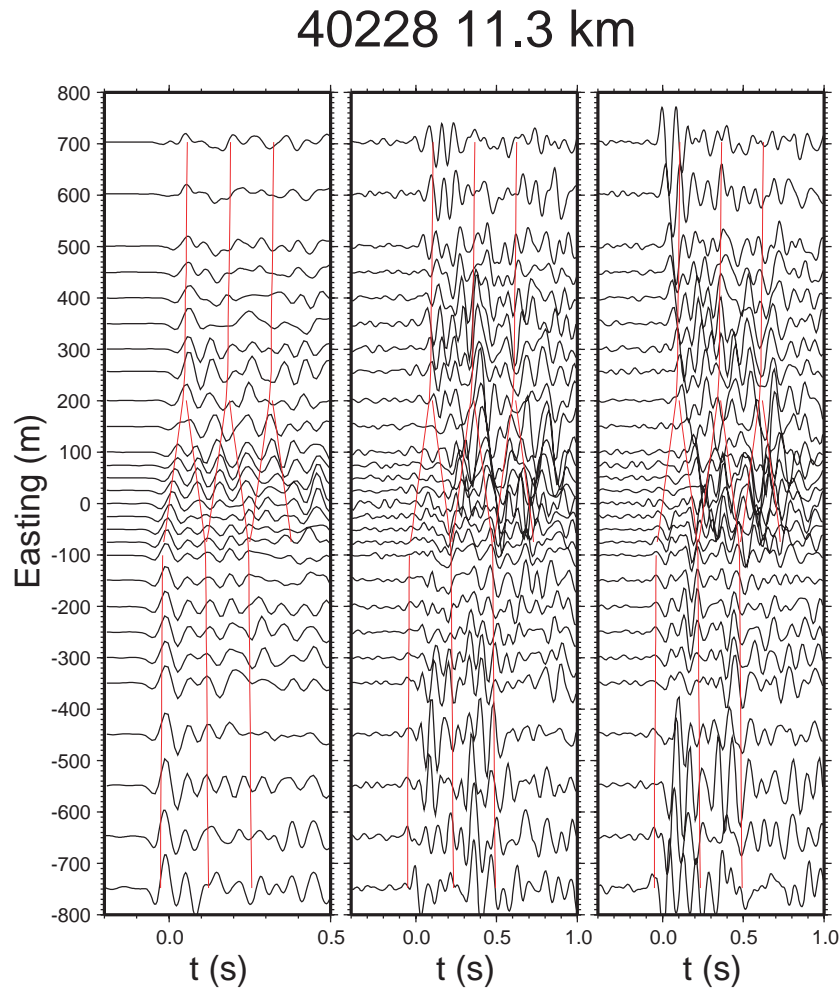
Figure 9. Waveform record sections of event 40228.

40228 shows a weak precursor to the direct *P* at the easternmost station (Fig. 9). These observations suggest that the low-velocity zone extends to a depth of ∼7 km.

4 DISCUSSION AND CONCLUSIONS

Near-vertical FZs are difficult targets to image using seismic methods. So far only a few successful cases using scattering waves generated by explosions have been reported (Louie *et al.* 1988; Hole *et al.* 2001; Maercklin *et al.* 2004). In rare occasions where deep borehole seismometers were available, earthquakes were also used as the energy source (Chavarria *et al.* 2003). In all cases, only the shallow portion (<4 km) of the FZs have been imaged. FZ head waves have also been identified on local earthquake recordings and used to determined FZ velocity contrast and its depth variation (Ben-Zion 1989; Ben-Zion & Aki 1990; Ben-Zion 1998; Hough *et al.* 1994; McGuire & Ben-Zion 2005). Our study demonstrates that reflections by near-vertical FZs are commonly recorded when stations and aftershocks are close to the FZ. Waveform record sections of the 1992 Landers aftershock recording experiment show that the reflected phases are stable and coherent at frequencies as high as 15 Hz. Their arrival times and amplitudes place new constraints on FZ structure at depth.

Until now, most results on FZ structures at depth were obtained by modelling FZ trapped waves. In our study area, Li *et al.* (2000) reported a depth-dependent FZ structure in which the FZ is 250 m wide with a 45 per cent velocity reduction at the surface and tapers to 125 m and 35 per cent reduction at 10 km depth. Peng *et al.* (2003), using the same data set, found that the seismic-wave-trapping structure in the Landers rupture zone has an effective width of ∼200 m with a 30–40 per cent *S*-wave velocity reduction down to a depth of 2–4 km, and $Q_s = 20$–30. Their study also demonstrated that there are strong trade-offs among different FZ parameters. This has also been recognized by other studies (e.g. Ben-Zion 1998; Li *et al.* 2000; Li & Vernon 2001). Our study shows that the trade-offs can be greatly reduced using FZ reflections. In particular, the trade-off between FZ width and velocities can be essentially eliminated by estimating them separately in waveform record sections.

A hotly debated issue is the depth extent of the low-velocity FZ that traps seismic waves. One group has suggested that it penetrates down to the base of the seismogenic zone (e.g. Li *et al.* 1994, 2000; Li & Vernon 2001; Li *et al.* 2004), while others have argued for a shallow trapping structure extending only to a depth of 3–5 km (e.g. Ben-Zion *et al.* 2003; Peng *et al.* 2003; Lewis *et al.* 2005). Numerical analysis showed that sources well outside and below shallow FZs can produce apparent trapped waves similar to those by sources inside or very close to deep FZs (Jahnke *et al.* 2002; Fohrmann

40553 3.9 km
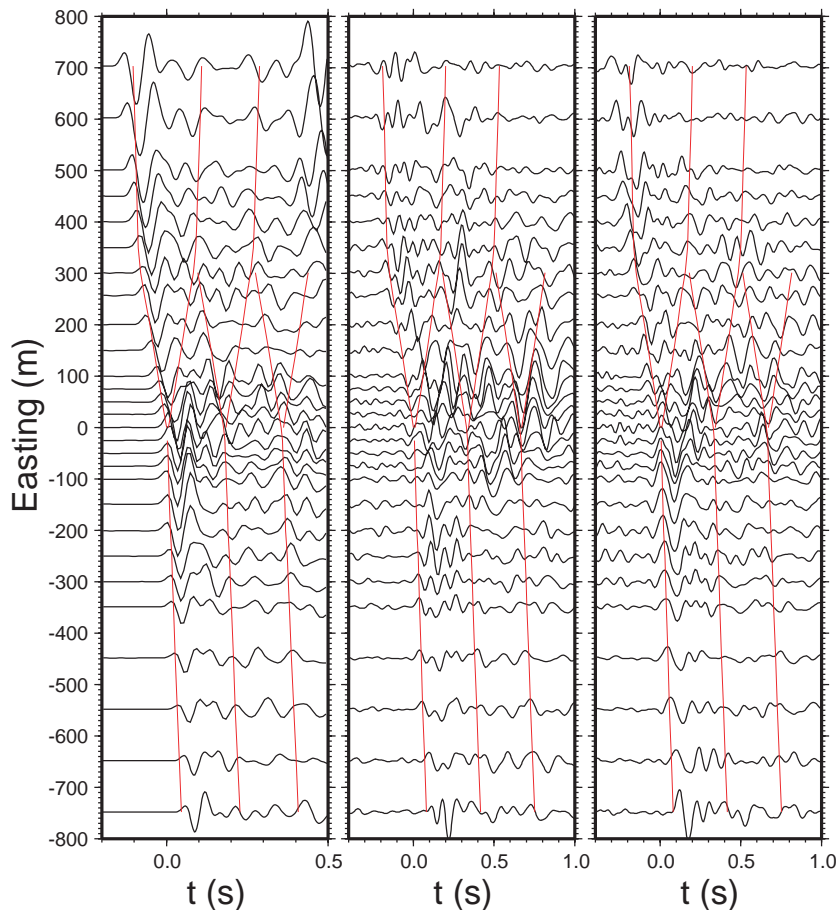
Figure 10. Waveform record sections of event 40553.

et al. 2004). Because the information brought up by trapped waves represents an integration of FZ properties over depth, they intrinsically lack depth resolution. In contrast, high-frequency FZ reflected phases have excellent spatial resolution because they sample the FZ at different locations depending on aftershock locations with respect to the FZ. We found that asymmetric waveform record sections from deep aftershocks that are close to the FZ can provide unequivocal constraints on the depth extent of the low velocity zone. Our waveform modelling of 10 Landers aftershocks suggests that the low-velocity zone of the Landers FZ extends to a depth of ∼7 km. It should be pointed out that this termination-depth estimate relies critically on the location accuracy of events used and FZ geometry. Given their uncertainties, we think that a range of depths, from 5 to 9 km, is possible. Therefore, our result is not necessarily in contrary with the previous shallow or deep estimates. A more detailed analysis of the *Q* value of the FZ may provide stronger constraints on the depth extent of the low velocity FZ layer.

The width and velocity reduction of the low-velocity zone determined in this study are consistent with but slightly larger than those of previous studies of trapped waves by Li *et al.* (2000) and Peng *et al.* (2003). We interpret the low-velocity zone to be the cumulative damaged zone caused by repeated earthquake ruptures along the fault over geological time. Studies of exhumed faults have shown that the typical width of damaged zones is on the order of sev-

eral hundreds of metres (e.g. Chester *et al.* 1993; Evans & Chester 1995; Chester & Chester 1998; Ben-Zion & Sammis 2003). Recent drilling of the San Andreas Fault near Parkfield has revealed a low-velocity zone of 250 m in width with a 20–30 per cent velocity drop at a depth of 3.2 km (Hickman *et al.* 2005). Possible mechanisms of reducing seismic velocities in the damaged zone include intense fracturing and pulverization, breciation, and fluid saturation. Our results show that the Landers FZ's *S*-velocity drops are consistently larger than the *P*-velocity drops (Table 1 and Fig. 14), suggesting that fluid saturation might be the main cause because it tends to reduce the *S* velocity more than the *P* velocity.

A major source of uncertainty of our results from modelling FZ reflected waves is location uncertainty of the aftershocks used. The small aperture (1.5 km) of the combined temporary array prevented us from accurately relocating the events. We used the relocation results of Shearer *et al.* (2005) that, on average, have a location uncertainty of less than 1 km. We improved focal depth determinations by using their *S–P* times at the temporary array, which is critical for estimating the depth extent of the low velocity zone, as noted by Peng *et al.* (2003). Based on the accuracy of our *S−P* time measurements (<0.05 s), we estimate that the focal depth uncertainty is less than 0.5 km. Such a location uncertainty, although relatively small, when coupled with the uncertainties in FZ strike and dip, can easily cause a couple of kilometres uncertainty in estimating

40028 5.4 km
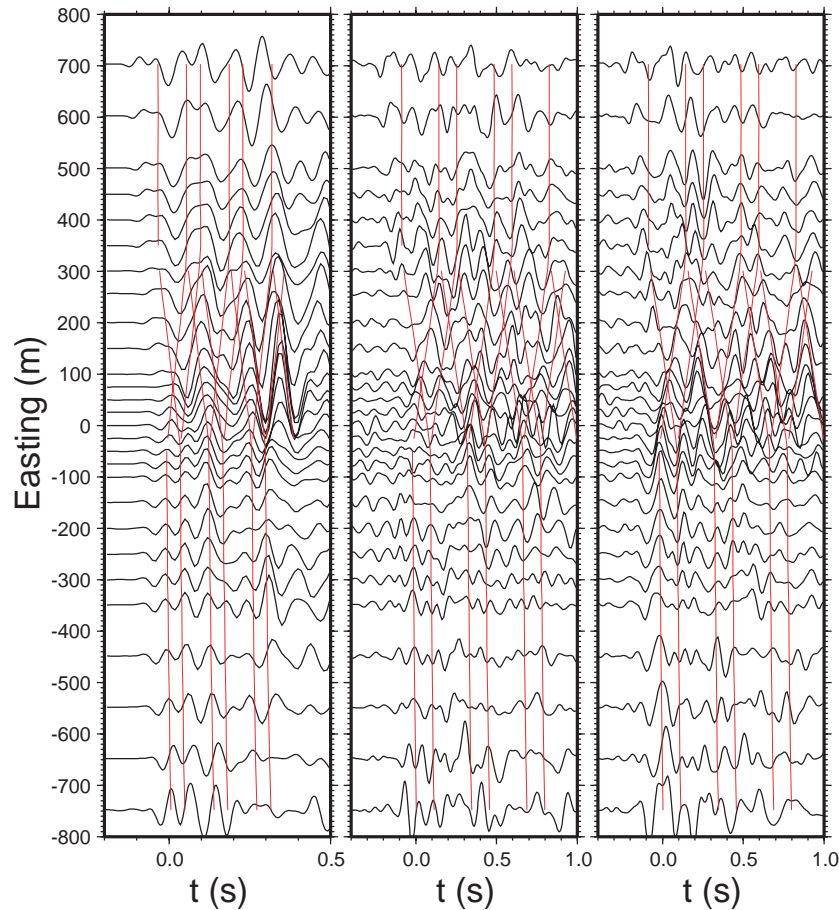
Figure 11. Waveform record section of event 40028.

the location of FZ reflection point. Future aftershock recording experiments should consider adding a few stations away from the FZ to provide the capability for locating aftershocks in places where station coverage by the permanent network is not sufficiently dense.

In conclusion, we have developed an efficient method for computing synthetic seismograms for arbitrarily oriented tabular FZ models based on GRT. Waveform record sections across a hypothetical vertical low-velocity FZ show that both arrival times and waveforms of *P* and *S* waves vary systematically across the FZ due to transmissions and reflections from boundaries of the low-velocity FZ. This allows us to determine the boundaries of the FZ, its *P*- and *S*-wave velocities, and the depth extent separately using waveform record sections from aftershocks that are close to the FZ. The trade-off between the FZ width and velocities is, therefore, avoided. Applying the method to high-frequency waveform data from the 1992 Landers aftershock recording experiment images a low-velocity FZ of 270–360 m wide with a 35–60 per cent reduction in *P* and *S* velocities relative to the host rock and a depth extent of ∼7 km. The western boundary of the low-velocity zone coincides with the observed main surface rupture trace.

REFERENCES

Aki, K., 1979. Characterization of barriers on an earthquak fault, *J. geophys. Res.,* **84,** 6140–6148.

Ben-Zion, Y., 1989. The response of two joined quarter spaces to SH line sources located at the material discontinuity interface, *Geophys. J. Int.,* **98,** 213–222.

Ben-Zion, Y., 1990. The response of two half spaces to point dislocations at the material interface, *Geophys. J. Int.,* **101,** 507–528.

Ben-Zion, Y., 1998. Properties of seismic fault zone waves and their utility for imaging low-velocity structures, *J. geophys. Res.,* **103,** 12 567–12 585.

Ben-Zion, Y. & Aki, K., 1990. Seismic radiation from an SH line source in a laterally heterogeneous planar fault zone, *Bull. seism. Soc. Am.,* **80,** 971–994.

Ben-Zion, Y. & Malin, P., 1991. San Andreas fault zone head wave near Parkfield, California, *Science,* **251,** 1592–1594.
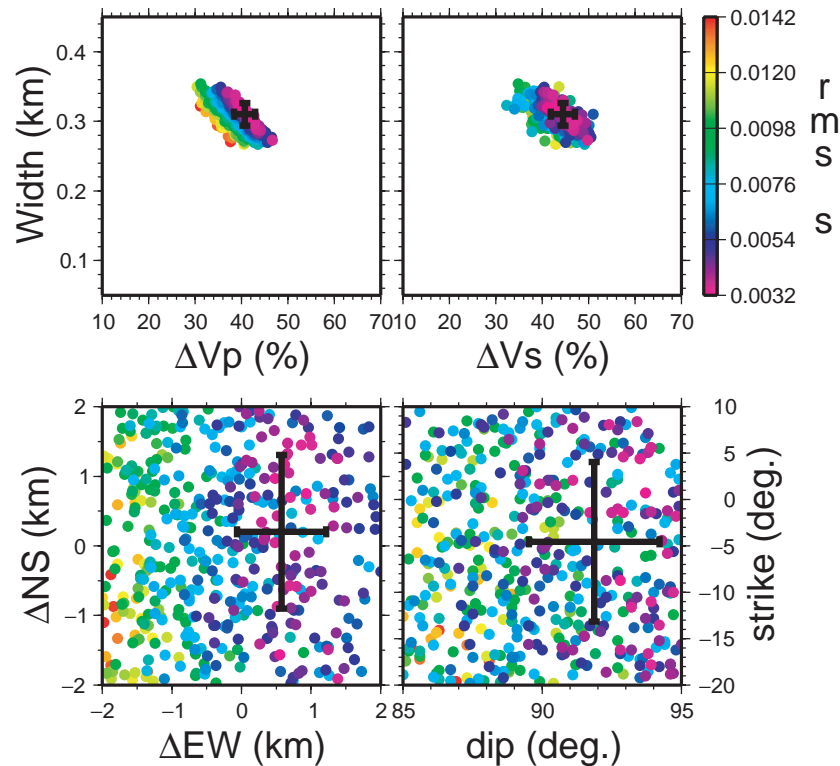
Figure 12. FZ width and *P* and *S* velocity drops as determined by least-squares inversions of arrival times of the direct and FZ-reflected *P* and *S* phases for event 40228. The inversion is repeated 500 times while randomly perturbing the event location, FZ strike, and dip. The 'optimal' parameters, obtained by a weighted average of all acceptable solutions, are indicated by the cross with its lengths equal to one standard deviation.

Table 1. Landers FZ strike, dip, width and velocity drops from the traveltime inversion.

Event	M_w	h (km)	Δ(km)	h_r (km)	strike (°)	dip (°)	y_0 (m)	width (m)	ΔV_P (per cent)	ΔV_S (per cent)
40028[a]	1.9	5.4	1.4	5.3	-8.2 ± 9.2	88.8 ± 2.5	-42 ± 6	365 ± 20	34 ± 2	49 ± 3
40034	2.2	10.9	4.5	3.4	-1.3 ± 8.0	89.7 ± 2.7	-42 ± 6	321 ± 13	48 ± 2	54 ± 3
40131	2.1	5.2	0.8	2.6	-4.4 ± 9.0	90.5 ± 2.7	-67 ± 6	285 ± 17	45 ± 3	49 ± 3
40228	2.4	11.4	1.9	5.3	-4.6 ± 8.6	91.9 ± 2.4	-87 ± 7	310 ± 16	41 ± 2	45 ± 3
40553	2.4	4.0	3.0	1.3	-2.3 ± 7.9	90.2 ± 2.9	-12 ± 7	342 ± 14	47 ± 2	50 ± 3
50829	1.8	4.0	1.6	2.5	-3.2 ± 8.7	90.3 ± 3.1	-60 ± 11	298 ± 17	53 ± 3	58 ± 4
50912	2.3	7.5	4.0	4.3	-6.5 ± 6.9	90.5 ± 2.7	-61 ± 10	279 ± 17	43 ± 3	59 ± 3
60511	2.6	7.2	1.9	3.4	-3.7 ± 8.3	90.6 ± 2.6	-58 ± 11	275 ± 18	37 ± 3	47 ± 3
61042[a]	1.7	5.3	5.4	5.3	-9.2 ± 8.4	90.3 ± 2.6	-60 ± 7	340 ± 13	38 ± 2	48 ± 4
71022[a]	1.8	9.5	3.1	9.4	-5.9 ± 7.2	93.0 ± 2.2	-67 ± 6	338 ± 13	40 ± 2	40 ± 2

[a]Indicates inside event; h: event depth; Δ: event epicentral distance to station C00; h_r: depth of the first FZ reflection point; y_0: FZ western boundary location relative to C00.

Ben-Zion, Y. & Sammis, C.G., 2003. Characterization of fault zones, *Pure appl. Geophys., 160,* 677–715.

Ben-Zion, Y. *et al.*, 2003. A shallow zone structure illuminated by trapped waves in the Karadere-Duze branch of the North Anatolian Fault, western Turkey, *Geophys. J. Int., 155,* 1021–1041.

Chavarria, J.A., Malin, P., Catchings, R.D. & Shalev, E., 2003. A look inside the San Andreas fault at Parkfield through vertical seismic profiling, *Science, 302,* 1746–1748.

Chester, F.M. & Chester, J.S., 1998. Ultracataclasite structure and friction processes of the Punchbowl fault, San Andreas system, California, *Tectonophysics, 295,* 199–221.

Chester, F.M., Evans, J.P. & Biegel, R.L., 1993. Internal structure and weakening mechanisms of the San Andreas fault, *J. geophys. Res., 98,* 771–786.

Evans, J.P. & Chester, F.M., 1995. Fluid-rock interaction in faults of the San Andreas system: inferences from San Gabriel fault rock geochemistry and microstructures, *J. geophys. Res., 100*(B7), 13 007–13 020.

Fohrmann, M., Igel, H., Jahnke, G. & Ben-Zion, Y., 2004. Guided waves from sources outside faults: an indication for shallow fault zone structure? *Pure appl. Geophys, 161,* 2125–2137.

Helmberger, D.V., 1983. Theory and application of synthetic seismograms, in *Earthquakes: Observation, Theory and Interpretation,* pp. 174–222, Soc. Italiana di Fisica, Bolgna, Italy.

Hickman, S.H., Zoback, M.D. & Ellsworth, W.L., 2005. Structure and composition of the San Andreas fault zone at Parkfield: initial results from SAFOD Phase 1 and 2, *EOS, Trans. Am. geophys. Un., 83*(47), 237.

Hole, J.A., Catchings, R., Clair, K.C.S., Rymer, M.J., Okaya, D.A. & Carney, B.J., 2001. Steep-dip seismic imaging of the shallow San Andreas Fault near Parkfield, *Science, 294,* 1513–1515.

Hough, S.E., Ben-Zion, Y. & Leary, P., 1994. Fault zone waves observed at the southern Joshua Tree earthquake rupture zone, *Bull. seism. Soc. Am., 84,* 761–767.

Jahnke, G., Igel, H. & Ben-Zion, Y., 2002. Three-dimensional calculations
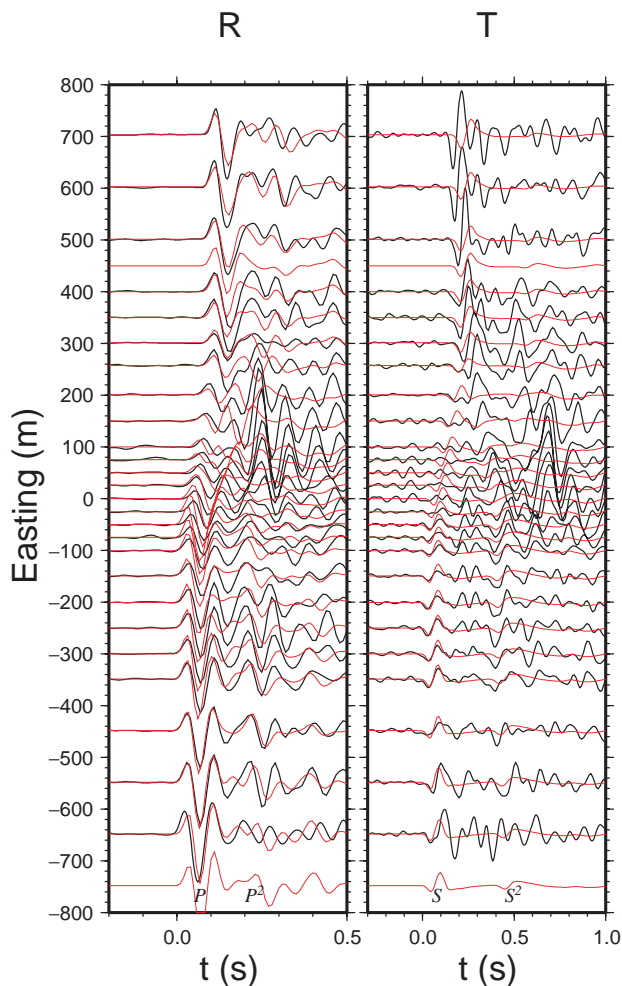
Figure 13. Comparison of synthetic waveform (red) and the observed seismograms (black) for event 40034. Horizontal axes show time after the earliest *P* (left-hand panel) and *S* arrival (right-hand panel).

of fault zone guided wave in various irregular structures, *Geophys. J. Int.,* **151,** 416–426.

Kanamori, H., 1994. Mechanics of earthquakes, *Ann. Rev. Earth Planet. Sci.,* **22,** 207–237.

Kanamori, H. & Brodsky, E.E., 2004. The physics of earthquakes, *Rep. Prog. Phys.,* **67,** 1429–1496.

Korneev, V.A., McEvilly, T.V. & Karageorgi, E.D., 2000. Seismological studies at Parkfield VIII: modeling the observed travel-time changes, *Bull. seism. Soc. Am.,* **90,** 702–708.

Lee, W.H.K., 1999. Digital waveform data of 238 selected Landers aftershocks from a dense PC-based seismic array, *Tech. rep.,* US Geol. Surv..

Lewis, M.A., Peng, Z.G., Ben-Zion, Y. & Vernon, F.L., 2005. Shallow seismic trapping structure in the San Jacinto fault zone near Anza, California, *Geophys. J. Int.,* **162,** 867–881.

Li, Y.G. & Leary, P.G., 1990. Fault zone trapped seismic waves, *Bull. seism. Soc. Am.,* **80,** 1245–1271.

Li, Y.G. & Vernon, F.L., 2001. Characterization of the San Jacinto fault zone near Anza, California, by fault zone trapped waves, *J. geophys. Res.,* **106,** 30 671–30 688.

Li, Y.G., Aki, K., Adams, D., Hasemi, A. & Lee, W.H.K., 1994. Seismic guided waves trapped in the fault zone of the Landers, California, earthquake of 1992, *J. geophys. Res.,* **99,** 11 705–11 722.

Li, Y.G., Vidale, J.E., Aki, K. & Xu, F., 2000. Depth-dependent structure of the Landers fault zone using fault zone trapped waves generated by aftershocks, *J. geophys. Res.,* **105,** 6237–6254.

Li, Y.G., Vidale, J.E. & Cochran, E.S., 2004. Low-velocity damaged structure of the San Andreas Fault at Parkfield from fault zone trapped waves, *Geophys. Res. Lett.,* **31,** L12S06, doi:10.1029/2003GL019,044.

Louie, J.N., Clayton, R.W. & Bras, R.J.L., 1988. 3-D imaging of steeply dipping structure near the San Andreas fault, Parkfield, California, *Geophysics,* **53,** 176–185.

Maercklin, N., Haberland, C., Ryberg, T., Weber, M., Bartov, Y. & the DESERT Group, 2004. Imaging the Dead Sea Transform with scattered seismic waves, *Geophys. J. Int.,* **158,** 179–186.

McGuire, J. & Ben-Zion, Y., 2005. High-resolution imaging of the Bear Valley section of the San Andreas fault at seismogenic depths with fault-zone head waves and relocated seismicity, *Geophys. J. Int.,* **162,** 1049.

Peng, Z., Ben-Zion, Y., Michael, A.J. & Zhu, L.P., 2003. Quantitative analysis of seismic fault zone waves in the rupture zone of the Landers, 1992, California earthquake: evidence for a shallow trapping structure, *Geophys. J. Int.,* **155,** 1021–1041.

Scholz, C.H., 1990. *The Mechanics of Earthquakes and Faulting,* Cambridge Univ. Press, New York.

Shearer, P., Hauksson, E. & Lin, G., 2005. Southern California hypocenter relocation with waveform cross-correlation, Part 2: results using source-specific station terms and cluster analysis, *Bull. seism. Soc. Am.,* **95,** 904–915, doi:10.1785/0120040168.

Sieh, K. *et al.*, 1993. Near-field investigations of the Landers earthquake sequence, April to July 1992, *Science,* **260,** 171–176.

Zhu, L. & Helmberger, D.V., 1996. Advancement in source estimation techniques using broadband regional seismograms, *Bull. seism. Soc. Am.,* **86,** 1634–1641.
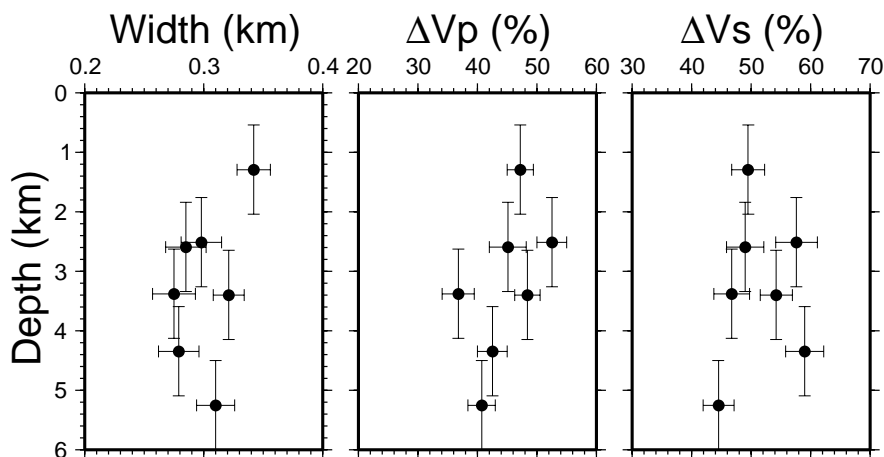
Figure 14. FZ widths, *P*- and *S*-velocity drops as a function of the depth of the first FZ reflection point from the outside events.